International Journal on Engineering, Science and Technology
Volume 3, Issue 2, 2021 ISSN: 2642-4088

Multidisciplinary Optimal Design of an Active Control System and State Estimator for an Aircraft Wing

Christopher Stephen Greer
Marshall University, USA

Yousef Sardahi
Marshall University, USA, sardahi@marshall.edu

Abstract: A multidisciplinary and multi-objective optimization approach that integrates the design of the control surfaces' sizes, active control system, and estimator for an aircraft's wing with three control surfaces is developed in this paper. Four objectives are considered: minimizing impacts of external gust loads, maximizing stability robustness, reducing control energy consumption, and minimizing the Frobenius norm of the estimator gains. For simulation purposes, a mathematical model of a flexible wing having three ailerons is used. The control system and observer are designed simultaneously. The optimization problem is formulated and solved by NSGA-II (non-dominated sorting genetic algorithm II). The solution of the optimization problem is called the Pareto set and the corresponding set of function evaluations is called Pareto front. The properties of the Pareto set and Pareto front; sensitives of the dominant poles of the open-loop system, closed-loop system, and estimator to the airspeed; and responses of the controlled, uncontrolled, and observer models at selected objective values are obtained. The results shows that the simultaneous design of the control and estimator algorithms, and the geometry of the ailerons in the multi-objective settings is very effective, the closed-loop control system can suppress the flutter and stabilize the system, and the estimator converges very quickly and always stable regardless of the air stream velocity.

Keywords: multidisciplinary and multi-objective optimization, control systems, observer design, flexible aircraft wings

Introduction

Multidisciplinary design of flexible structures such as aircraft wings has helped improve their performance in the past. During the design, wing's geometrical parameters and control gains are varied to simultaneously satisfy multiple and often conflicting requirements. Design objectives such as maximizing the stability of the aeroelastic structures, suppression of instabilities, robustness against gust loads and measurement noise, and minimizing energy consumption are critically important when designing active aeroelastic controls. Therefore, additional work on the subject can further improve their performance by combining the concept of multidisciplinary design with that of multi-objective optimization.

There have been a few research efforts in the field of multidisciplinary optimal design (MOD) of aircraft wings. For example, an MOD of an aircraft wing was investigated by (Khot, Appa, and Eastep, 2000) to enhance a wing roll performance at high dynamic pressures. The structure of the wing was optimized first to obtain a feasible flexible wing. Then, an optimal control design was conducted to determine the distribution of actuators' forces. Singh and his colleagues formulated two optimization problems (Singh & McDonough, 2014). In the first problem, the chord fraction of an aileron attached to a wing was selected as the tuning parameter. In the second problem, only the span-wise length of the first control surface of a wing having multiple control surfaces was selected as the design variable. In both problems, the optimization goal was to minimize the control system energy through minimizing the norms of the control gains while satisfying some constraints on closed-loop poles, which define the extension of the open loop flutter boundary. Likewise, Brown and Singh optimally adjusted the locations, span-wise lengths, and chord sizes of a leading and trailing edge control surface under static constraints related to the size of the control surfaces as well as dynamic constraints related to the active pole placement for flutter boundary extension (Brown & Singh, 2015). In another study, (Brown, Singh, & Kolonay, 2017) used genetic algorithms to tune the size, location, and number of leading and trailing control surfaces of a fighter wing model. The optimization goal was to achieve an active aeroelastic control for flutter boundary extension with minimum control effort. Therein, two cases were considered. In the first optimization problem, the number of control surfaces was fixed while their chords, span lengths, and locations were tuned. In the second optimization problem, the number and locations of control surfaces were tuned while their sizes were fixed. In another work, a series of aeroelastic optimization problems for a subsonic transport wing under a

variety of static and dynamic constraints was solved by (Stanford, 2016). In one of these optimization problems, the mass of the wing was minimized by simultaneously tuning its structural variables (skin thickness, stiffener details), the quasi-steady deflection scheduling of a series of control surfaces distributed along the trailing edge for maneuver load alleviation and trim attainment, and the design details of a Linear Quadratic Regulator (LQR). By the same token, Nam, Chattopadhyay, and Kim (2000) employed genetic algorithms for an integrated simultaneous aeroservoelastic design of a composite aircraft wing. Eight design variables consisting of the ply orientation of the composite layer, wing sweep angle, taper ratio, aspect ratio, span wise location, and size of the control surfaces were selected as design parameters. The objective function was defined as a weighted sum of 25 index values, which are LQR performance index based on an output feedback controller at a design airspeed and the root mean square values of the gust responses for various airspeeds. The results showed considerable improvements in both objectives when the optimized models were compared to baseline models. Another MOD was presented by (Haghighat, Martins, & Liu, 2012). Therein, the main design goal was to maximize the endurance of a high-altitude long endurance aircraft by tuning wing planform parameters (wing area and span-wise twist distribution), structural sizing (spar-wall thicknesses), and control gains (diagonal elements of the state weighting matrix of the LQR algorithm) concurrently. The results showed that the simultaneous design of the control system along with structure of the wing at the early stages of aircraft design improves the aircraft performance.

In this paper, we go one step further and introduce a multidisciplinary and multi-objective optimization approach that integrates the design of the control surfaces' sizes, active control system, and estimator for an aircraft's wing having three control surfaces. Four objectives are considered: minimizing impacts of external gust loads, maximizing stability robustness, reducing control energy consumption, and minimizing the Frobenius norm of the estimator gains. A mathematical model of a flexible aircraft wing used for numerical simulations is introduced in the next sections.

Mathematical Model of an Aircraft's Wing with Multiple Control Surfaces

Consider the flexible wing with three control surfaces shown in Figure 1. The matrix-differential equation governing the dynamic of the system is given by

$$\mathbf{M}\ddot{\mathbf{q}}(t)+\left(\mathbf{C}-\rho V\mathbf{C_a}\right)\dot{\mathbf{q}}(t)+\left(\mathbf{K}-\rho V^2\mathbf{K_a}\right)\mathbf{q}(t)=\mathbf{F_c}\mathbf{u}(t)+\mathbf{F_g}\mathbf{w_g}(t) \quad (1)$$

The vector $\mathbf{q}(t)=\left[q_1(t),...,q_4(t)\right]^T$ represents the generalization coordinate, $\mathbf{u}(t)=\left[\beta_1(t),...,\beta_3(t)\right]^T$ denotes the vector of the control surface deflection as labeled in the figure, $\mathbf{F_c}$ is the matrix describing the influence of the controls on the system dynamics, and $\mathbf{F_g}$ describes the influence of aerodynamic loads, $\mathbf{w_g}$(t), on the system behavior. The matrices $\mathbf{M}$, $\mathbf{C_a}$, $\mathbf{C}$, $\mathbf{K_a}$, and $\mathbf{K}$ are the structural inertia, aerodynamic damping, structural damping, aerodynamic stiffness, and structural stiffness matrices, respectively. The reader can refer to Appendix A or more details about the model and the numerical values (see Table A.1) used in the simulation.

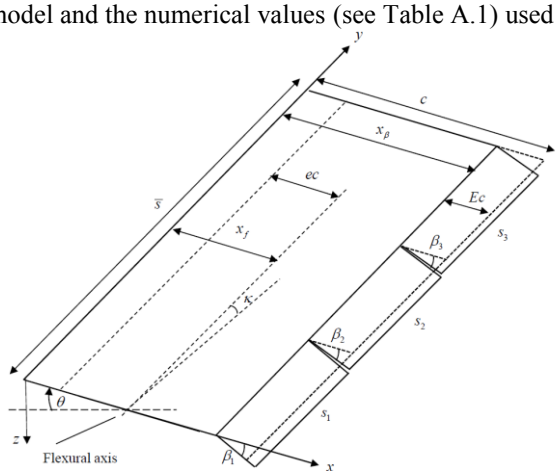

Figure 1. Flexible Aircraft Wing Model with Three Control Surfaces (Singh & McDonough, 2014)

The bending deformation (transverse direction) z and rotation θ at a point (x, y) on the wing are related to the generalized coordinates and the wing's dimensions by the following equations:

$$z(t)=y^2q_1(t)+y^3q_2(t)+y(x-x_f)q_3(t)+y^2(x-x_f)q_4(t) \quad (2)$$

$$\theta(t) = yq_3(t) + y^2 q_4(t) \tag{3}$$

where, x_f is the flexural axis location aft of leading edge.

Optimal Full-State Feedback Control System

The state-space model of the system described in Eq. (1) reads

$$\dot{\mathbf{x}}(t) = \mathbf{A}\mathbf{x}(t) + \mathbf{B}_\mathbf{u}\mathbf{u}(t) + \mathbf{B}_\mathbf{g}\mathbf{w}_\mathbf{g}(t). \tag{4}$$

The output equation is given by

$$\mathbf{y}(t) = \mathbf{C}_\mathbf{o}\mathbf{x}(t). \tag{5}$$

Where, $\mathbf{x}(t) = \left[q_1(t),...,q_4(t),\dot{q}_1(t),...,\dot{q}_4(t)\right]^T$ is the state vector. The system matrices **A**, $\mathbf{B}_\mathbf{u}$, $\mathbf{B}_\mathbf{g}$, and $\mathbf{C}_\mathbf{o}$ read

$$\mathbf{A} = \begin{bmatrix} \mathbf{0}_{4\times4} & \mathbf{I}_{4\times4} \\ -\mathbf{M}^{-1}\left(\mathbf{K} - \rho\mathbf{V}^2\mathbf{K}_\mathbf{a}\right) & -\mathbf{M}^{-1}\left(\mathbf{C} - \rho\mathbf{V}\mathbf{C}_\mathbf{a}\right) \end{bmatrix} \tag{6}$$

$$\mathbf{B}_\mathbf{u} = \begin{bmatrix} \mathbf{0}_{4\times3} \\ \mathbf{M}^{-1}\mathbf{F}_\mathbf{c} \end{bmatrix} \tag{7}$$

$$\mathbf{B}_\mathbf{g} = \begin{bmatrix} \mathbf{0}_{4\times3} \\ \mathbf{M}^{-1}\mathbf{F}_\mathbf{g} \end{bmatrix} \tag{8}$$

$$\mathbf{C}_\mathbf{o} = \begin{bmatrix} \mathbf{I}_{4\times4} & \mathbf{0}_{4\times4} \end{bmatrix} \tag{9}$$

Where, **I** and **0** denote the identity and zero matrices, respectively. It is evident from the system configuration that the system is completely controllable. Also, the system is completely observable. That is, with the on-board sensors' distribution given in Eq. (9), the first four states can be measured directly and then used to estimate the last four states. A MIMO full-state feedback law for the state-space system given in Eq. (4) can be written as

$$\mathbf{u}(t) = -\mathbf{K}_\mathbf{c}\mathbf{x}(t). \tag{10}$$

where, $\boldsymbol{K_c} \in \mathbb{R}^{3\times8}$ is the state feedback gain matrix. Substituting Eq. (10) into Eq. (4), the closed-loop dynamics is given by

$$\dot{\mathbf{x}}(t) = \left(\mathbf{A} - \mathbf{B}_\mathbf{u}\mathbf{K}_\mathbf{c}\right)\mathbf{x}(t) + \mathbf{B}_\mathbf{g}\mathbf{w}_\mathbf{g}(t). \tag{11}$$

Taking the Laplace of Eq. (11), we obtain

$$\left(s\mathbf{I} - \mathbf{A} + \mathbf{B}_\mathbf{u}\mathbf{K}_\mathbf{c}\right)\mathbf{X}(s) = \mathbf{B}_\mathbf{g}\mathbf{W}_\mathbf{g}(s), \tag{12}$$

where, **X(s)** and $\mathbf{W}_\mathbf{g}$(s) are the Laplace transforms of **x(t)** and $\mathbf{w}_\mathbf{g}$(t), respectively. Using this equation and Eq. (5), the transfer function matrix **GTF(*s*)** from the gust loads to the system's outputs is provided by

$$\frac{\mathbf{Y}(s)}{\mathbf{W}_\mathbf{g}(s)} = \mathbf{C}_\mathbf{o}\left(s\mathbf{I} - \mathbf{A} + \mathbf{B}_\mathbf{u}\mathbf{K}_\mathbf{c}\right)^{-1}\mathbf{B}_\mathbf{g}. \tag{13}$$

Here, **Y**(s) denotes the Laplace transform of **y**(t). This transfer function matrix is very crucial in the design of the control system since one of the design requirements is to alleviate the impacts of extreme aerodynamic loads on the system performance. It is evident from this equation that by increasing $\mathbf{K}_\mathbf{c}$, the gust loads' effects can be reduced. However, this conflicts with the requirement of minimizing the control energy needed to stabilize the system and suppress flutter. Also, the span-wise lengths (s_1, s_2, and s_3) and chord width (E_c) labeled in Figure 1 play very important rule in the ability of the system to reject gust loads since they decide the values of $\mathbf{B}_\mathbf{u}$ and $\mathbf{B}_\mathbf{g}$ as shown in the Appendix. This emphasises the important of handling the design in multi-objective and multidisciplinary settings.

Linear- Quadratic Regulator (LQR) Design

The state feedback gain matrix $\mathbf{K}_\mathbf{c}$ can be either directly tuned if the stable ranges of its elements are known, or indirectly computed by solving the Algebraic Riccati Equation (ARE) which results in an LQR. The latter is very attractive since it does not require any stability analysis and the user only needs to adjust some weighting

factors and then numerically solve the ARE to obtain $\mathbf{K_c}$. In this case, $\mathbf{K_c}$ minimizes the following performance index:

$$J = \int_0^\infty \left(\mathbf{x}^T(t)\mathbf{Q}\mathbf{x}(t) + \mathbf{u}^T(t)\mathbf{R}\mathbf{u}(t) \right) dt. \tag{14}$$

Where $\mathbf{Q} = \mathbf{Q}^T$ is a positive semidefinite matrix that penalizes the departure of system states from the equilibrium, and $\mathbf{R} = \mathbf{R}^T$ is a positive definite matrix that penalizes the control input. Using Lagrange multiplier-based optimization method, the optimal $\mathbf{K_c}$ is given by

$$\mathbf{K_c} = \mathbf{R}^{-1}\mathbf{B_u}\mathbf{P} \tag{15}$$

The matrix $\boldsymbol{P} \in \mathbb{R}^{8\times 8}$ can be calculated by solving the following ARE:

$$\mathbf{A}^T\mathbf{P} + \mathbf{P}\mathbf{A} - \mathbf{Q} - \mathbf{P}\mathbf{B_u}\mathbf{R}^{-1}\mathbf{B_u}^T\mathbf{P} = 0 \tag{16}$$

It is evident from Eqs. (15) and (16) that $\mathbf{Q}$ and $\mathbf{R}$ are the design knobs that greatly impact the calculation of $\mathbf{K_c}$ and in turn the performance of the system under control. Thus, the most important step in the design of an optimal controller using LQR is the choice of $\mathbf{Q}$ and $\mathbf{R}$ matrices. Conventionally, these matrices are elected based on the designer's experience and adjusted iteratively to obtain the desired performance. Arbitrary selection of $\mathbf{Q}$ and $\mathbf{R}$ will result in a certain system response which is not optimal in true sense (Tewari, 2002). Many efforts have been directed toward developing systematic methods for selecting the weighting matrices. For instance, Bryson presented an approach for choosing the starting values of $\mathbf{Q}$ and $\mathbf{R}$ matrices, but this method only suggests the initial values and later the coefficients are to be tuned iteratively for optimal performance (Bryson, 2018). Analytical approach of selecting the $\mathbf{Q}$ and $\mathbf{R}$ matrices for a second order crane system was developed by (Oral, Çetin, & Uyar, 2010). Another analytical method of calculating the $\mathbf{Q}$ and $\mathbf{R}$ matrices for a third order system represented in the control canonical form was proposed by (El Hajjaji & Ouladsine, 2001). Developing an analytical technique to find $\mathbf{Q}$ and $\mathbf{R}$ for high order systems such as the system at hand is very tedious if it is not possible because of the dimension of the system. Therefore, we suggest a numerical approach through using an optimization algorithm to tune these matrices such that the design goals are optimized simultaneously.

The LQR does not only guarantee the system stability but also the stability margins. This feature is very valuable for high-order dynamic systems where finding the feasible regions of the control gains are very difficult. On the other side, LQR requires that you have a good model of the system, and all the states in the system available for feedback. If not all the states are available, an observer should be used to estimate the unavailable ones. As a result, stability margins may get arbitrarily small. To avoid this situation, the estimator dynamics should be faster than the closed-loop dynamics i.e., the estimator eigenvalues should not be closer to the imaginary axis than those of the regulator. This can be done free of cost since the estimator does not require an actual control input (Tewari, 2002). As a result, the estimator poles can be pushed further into the left-half plan without causing concern of large control effort.

Luenberger Observer

Practically speaking, only a subset of states is available for feedback when the control system is designed. A cost-effective approach to determine the states that are not directly measured is to design an observer, which is nothing but a computer algorithm that uses the system mathematical model, available measurements, and feedback control signals to provide an estimate of the unavailable states. Luenberger observer is one of the popular and traditional estimators that can be used for this end (Luenberger, 1964). The dynamics of the Luenberger observer of the state-space system given in Eq. (4) assuming $\mathbf{B_g}\mathbf{w_g}(t)$ is unknown reads

$$\dot{\hat{\mathbf{x}}}(t) = \mathbf{A}\hat{\mathbf{x}}(t) + \mathbf{B_u}\mathbf{u}(t) + \mathbf{L}\left[\mathbf{y}(t) - \hat{\mathbf{y}}(t)\right] \tag{17}$$

$$\hat{\mathbf{y}}(t) = \mathbf{C_o}\hat{\mathbf{x}}(t). \tag{18}$$

The term $\mathbf{L}\left[\mathbf{y}(t) - \hat{\mathbf{y}}(t)\right]$ injects the error between measurements $\mathbf{x}(t)$ and model predictions $\hat{\mathbf{x}}(t)$, scaled by a user-chosen observer gain vector $\mathbf{L} \in$ ¡ $^{8\times 4}$. Letting $\mathbf{e}(t) = \mathbf{x}(t) - \hat{\mathbf{x}}(t)$, the error dynamics is governed by the following equation

$$\dot{\mathbf{e}}(t) = (\mathbf{A} - \mathbf{L}\mathbf{C_o})\mathbf{e}(t) \tag{19}$$

By examining this equation, we notice that the estimation error system is asymptotically stable, $\mathbf{e}(t)\rightarrow 0$, if we select $\mathbf{L}$ such that the eigenvalues of $(\mathbf{A}-\mathbf{LC_o})$ have negative real parts. That is, we can assign the eigenvalues (i.e., speed) of the error system by selecting $\mathbf{L}$ appropriately. Furthermore, the selection of $\mathbf{L}$ comes free of cost since the estimator does not require any form of physical control effort. As a result, the eigenvalues of the estimator λ_e can be placed to the left of the fastest mode of the closed-loop system, $\lambda_{c_{\min}}$ as follows

$$\lambda_e = r\times(1:8)\lambda_{c_{\min}} \tag{20}$$

where, $\lambda_{c_{\min}} = \min\left(real\left(eig\left(\mathbf{A}-\mathbf{B_u}\mathbf{K_c}\right)\right)\right)$ and $r \geq 2$ can be tuned to find the optimal trade-offs between the observer speed of response and noise amplifications, which are directly related to the values of $\mathbf{L}$. It can be noticed that $\lambda_{c_{\min}}$ is scaled by $r\times(1:8)$ to avoid placing the estimator poles at the same location since the pole placement can be badly conditioned if the designer picks out unrealistic pole locations (MathWork, 2020). The proposition in Eq. (20) is introduced in this paper to avoid such situation though other setups are also possible. Then, the MATLAB command "place" can be used to calculate $\mathbf{L}$.

Multi-Objective Optimization

Multi-objective optimization problems (MOPs) are stated as follows:

$$\min_{\mathbf{k}\in D}\left\{\mathbf{F}(\mathbf{k})\right\}. \tag{21}$$

Where a design variable vector $\mathbf{k}=[k_1,\ldots,k_n]$ must be found to minimize a vector $\mathbf{F}(\mathbf{k})=\left[f_1(\mathbf{k}),\ldots,f_m(\mathbf{k})\right]$. The domain $D\subset\mathbb{R}^n$ can in general be expressed by l inequality and q equality constraints:

$$D=\begin{Bmatrix}\boldsymbol{k}\in\mathbb{R}^n|g_i(\boldsymbol{k})\leq 0, i=1,\ldots,l\\ and\quad h_i(\boldsymbol{k})=0, j=1,\ldots,q\end{Bmatrix}. \tag{22}$$

The solution of a MOP is known as the Pareto set and its image is called the Pareto front. Therefore, the concept of dominancy (Pareto, 1971) is used to define the optimal solutions. Such solutions are non-dominated to each other. Simply stated, there exists no other solutions in the entire search space which dominate any of these solutions. MOPs are solved by multi-objective optimization algorithms which can be classified as evolutionary-based and gradient-based algorithms. The reader can refer to (Tian, Y., Cheng, R., Zhang, X., & Jin, Y., 2017) for a comprehensive survey of MOP algorithms.

Control systems' design problems are complicated and non-convex, therefore evolutionary algorithms are the methods of choice (Woźniak, 2010). They outperform classical direct and gradient-based methods which suffer from the following problems: 1) the convergence to an optimal solution depends on the initial solution supplied by the user, and 2) most algorithms tend to get stuck at a local or suboptimal solution when solving non-convex, and complex problems. On the other side, evolutionary algorithms are computationally expensive (Hu, Huang, & Wang, 2003). However, the computational cost can be justified if a more accurate solution is desired, and the optimization is conducted offline. The most widely used multi-objective optimization algorithm is the NSGA-II (Sardahi, Y. and Boker, A., 2018). It yields a better Pareto front as compared to SPEA2 (strength Pareto evolutionary algorithm) and PESA-II (Pareto Envelope based Selection Algorithm). Therefore, in this paper, we use the NSGA-II to solve the multi-objective optimal control problem at hand. The reader can refer to (Sardahi, 2016) for more details about the working principle of this algorithm. NSAG-II works well on two-objective and three-objective problems. For many objective optimization problems (with more than three objectives), large populations are used to enhance the searchability of the algorithm but at the expense of the computation time (Ishibuchi, 2009). A study on the effect of the size of the decision variable space on the performance of NSGA-II and other evolutionary algorithms showed that NSGA-II converges to the true Pareto front on all benchmark problems when the number of design parameters is less than or equal to 128 (Durillo, Nebro, Coello, Luna, & Alba, 2008). In this work, the size of the objective space is 4 and that of decision variable space is 15. Therefore, NSGA-II is expected to perform well in solving the optimization problem at hand.

Multi-objective and Multidisciplinary Optimal Design

Three pieces of information are needed for any optimization problem. They are the tunable parameters, fitness functions, and constraints. The design parameter space $\mathbf{k}$ (see Eq. (21)) is given by

$$\mathbf{k}=\left[Q_1,\ldots,Q_8,R_1,\ldots,R_3,\alpha_1,\alpha_2,E_c,r\right]. \tag{23}$$

The parameters $Q_1,\ldots,Q_8$, are the values on the main diagonal of **Q**, and $R_1,\ldots,R_3$ are the elements on the main diagonal of **R**. These variables are numerically adjusted to optimally tune $\mathbf{K_c}$. The span lengths and chord of the ailerons are also tuned by varying α_1, α_2, and E_c. Where α_1 and α_2 set the length of first ($s_1 = \alpha_1 \bar{s}$)and second ($s_2 = \alpha_2 \bar{s}$) aileron. Having the values of s_1 and s_2, the length of the third aileron can be simply calculated $s_3 = \left(\bar{s} - \left(s_1 + s_2\right)\right)$. It is worth noting that by changing α_1, α_2, and E_c, the sizes of the control surfaces are accordingly tuned, which decide both the amount of control energy and the ability of the closed loop to reject external aerodynamic loads. The reader can inspect the elements of the control and gust loading influence matrices $\mathbf{F_c}$ and $\mathbf{F_g}$ given in Appendix A to see how α_1, α_2, and E_c enter these matrices. The variable r dictates the locations of the estimator's poles relative to the further left pole of the closed-loop system, and in turn the speed of response of the observer. These design knobs were tuned to minimize the following design objectives

$$\min_{\mathbf{k}\in D}\left\{\lambda_{c_{\max}}, \left\|\mathbf{GTF}(j\omega)\right\|_\infty, \left\|\mathbf{B_u K_c}\right\|_F, \left\|\mathbf{L}\right\|_F\right\}. \tag{24}$$

The relative stability of the controlled system is expressed by $\lambda_{c_{\max}}$,where $\lambda_{c_{\max}} = \max\left(real\left(eig\left(\mathbf{A}-\mathbf{B_u K_c}\right)\right)\right)$ represent the real parts of eigenvalues of the closed-loop dynamic matrix. Small values of $\lambda_{c_{\max}}$ indicate better stability robustness of the controlled system. The fitness function $\|\mathbf{GTF}(j\omega)\|_\infty$ describe the disturbance rejection capability of the closed-loop system to gust loads. A general definition of $\|\mathbf{GTF}(j\omega)\|_\infty$ is given by

$$\left\|\mathbf{GTF}(j\omega)\right\|_\infty = \sup_{\omega\in\left[\omega_i,\omega_f\right]} \sigma\left(\mathbf{GTF}(j\omega)\right). \tag{25}$$

Where σ is the largest singular value among the transfer function elements. That is, the maximum value of $\|\mathbf{GTF}(j\omega)\|_\infty$ is minimized. The values of ω_i and ω_f are set to 0 and 1000, respectively, as suggested by (Singh & McDonough, 2014) . For a controlled system to have a good disturbance rejection, we must have $\|\mathbf{GTF}(j\omega)\|_\infty << 1$. The third objective, $\|\mathbf{B_u K_c}\|_F$, is the Frobenius norm of the control matrix given by

$$\left\|\mathbf{B_u K_c}\right\|_F = \sqrt{\sum_{j=1}^{8}\sum_{i=1}^{8}\left|m_{ij}\right|^2}. \tag{26}$$

where m_{ij} are the elements of $\mathbf{B_u K_c}$. Generally speaking, the minimization of this norm leads to minimization of the control energy, which is one of the design objectives in this work. The fourth fitness function $\|\mathbf{L}\|_F$, is the Frobenius norm of the estimator gain matrix and it is defined by

$$\left\|\mathbf{L}\right\|_F = \sqrt{\sum_{j=1}^{8}\sum_{i=1}^{4}\left|l_{ij}\right|^2}. \tag{27}$$

where l_{ij} are the elements of **L**. Small values of this cost function leads to slow estimator dynamics but less noise amplification, and vice versa.The MOP in Eq. (25) is solved by tuning the elements of **k** in Eq. (23) under the following constraints

$$D = \left\{\begin{array}{l} \boldsymbol{k} \in \mathbb{R}^{15} \mid Q_i \in [0{,}100], i = 1,\ldots.,8 \\ \quad R_j \in [0.0001{,}100], j = 1,\ldots.,3 \\ \quad \alpha_1, \alpha_2 \in [0.01{,}0.98], \\ \quad E_c \in [0.01{,}0.5], \\ \quad r \in [2{,}10] \end{array}\right\}. \tag{28}$$

Here, D denotes the feasible search space. The upper bounds on Q_i, R_j are chosen so that the penalties on the departures of the states from their desired positions and control utilization is high. The upper and lower limits of α_1 and α_2 suggest that the fractional lengths of the three control surfaces range from 1% to 98% of the airfoil span length. In contrast to the work proposed by (Singh & McDonough, 2014) where α_1 was constrained between 1% and 25% and the lengths of the second and third control surfaces were fixed, this wider ranges expand the domain of the search space in the direction of α_1 and α_2 and add another degree of freedom to the design space. The geometric constraint on the control surface chord fraction E_c is chosen according to the work presented in (Singh & McDonough, 2014). A relationship between the design objectives can be achieved by tuning the individual weights Q_i, R_j, and the control surfaces' widths and lengths. The design variable r was chosen between 2 and 10 to ensure the estimator is at least two times faster than the fastest closed-loop mode and at most 10 times faster.

To solve this multi-optimization problem, NSGA-II is used. There is no specific guide on how to set up the number of populations and generations for this algorithm. However, according to the MATLAB documentation, the population size can be set in different ways and the default population size is 15 times the number of the design variables n. Also, the maximum number of generations should not be greater than $200n$. In this study, the

population size and the number of iterations is set to *50n*. The MOP is solved at *V = 87.5m/s*, which marks the beginning of flutter and open-loop's instability.

Results and Discussion

The properties of the Pareto set and Pareto front; sensitive of the dominant poles of the open-loop system, closed-loop system, and estimator to the airspeed; and responses of the controlled, uncontrolled, and observer models at selected objective values are discussed here.

The optimization problem at hand is 15*4. That is, 15 decision variables and 4 objectives. So, it is difficult to depict all the objectives in one graph. Instead, 2D projections from the 4D design space are produced as shown in Figures 2, 3, and 4. The color in these two figures is mapped to the value of the objective $\|\mathbf{B_u K_c}\|_F$ with red denotes the highest value, and dark blue denotes the lowest value. It is evident from these figures that there is a competing relationship among the design objectives. For instance, by inspecting the subplots (a) and (b) of Figure 2, we note that at the maximum stability robustness $\lambda_{c_{\max}} = -31.0577$, $\|\mathbf{B_u K_c}\|_F$ and $\|\mathbf{L}\|_F$ read 2.5633e+06 and 9.6214e+07, respectively. While, at the minimum stability robustness $\lambda_{c_{\max}} = -10.1686$, $\|\mathbf{B_u K_c}\|_F$ and $\|\mathbf{L}\|_F$ read 3.0799e+05 and 4.7418e+06, respectively. Another example can be found in Figure 3. We notice that at the best disturbance rejection $\|\mathbf{GTF}(j\omega)\|_\infty$= 0.0011, $\|\mathbf{B_u K_c}\|_F$ and $\|\mathbf{L}\|_F$ read 2.4639e+06 and 9.2596e+ 07, respectively. While, at the worst gust loads' rejection $\|\mathbf{GTF}(j\omega)\|_\infty$= 0.0057, $\|\mathbf{B_u K_c}\|_F$ and $\|\mathbf{L}\|_F$ read 2.3481e + 04 and 5.6637e+ 06, respectively. That is, better disturbance rejection and stability robustness can be achieved by high control energy and estimator gain. High estimator gains may lead to high measurement noise amplifications. A third example is shown in Figure 4 where there is a conflict between the objective of minimizing the control energy consumption and that of attenuating sensors' noise amplification. Small values of $\|\mathbf{B_u K_c}\|_F$ and $\|\mathbf{L}\|_F$ are required to reduce the impact of measurement noise on the closed-loop performance as indicated by the dark blue region. On the other side, small energy levels mean bad aerodynamic load repudiation. As a result, the decision-maker should choose the solution that gives the best compromise between these objectives.

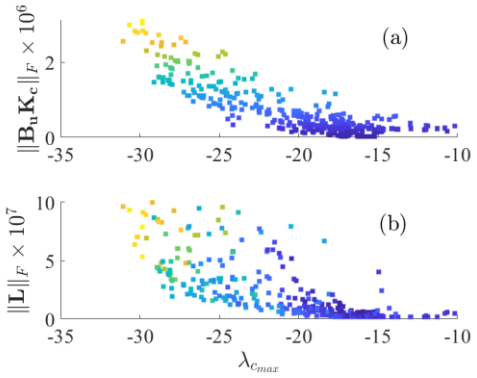

Figure 2. Projections of the Pareto Front. (a) $\|\mathbf{B_u K_c}\|_F$ versus $\lambda_{c_{\max}}$, (b) $\|\mathbf{L}\|_F$ versus $\lambda_{c_{\max}}$. The color code represents the levels of $\|\mathbf{B_u K_c}\|_F$ with red denotes the highest value, and dark blue denotes the lowest value.

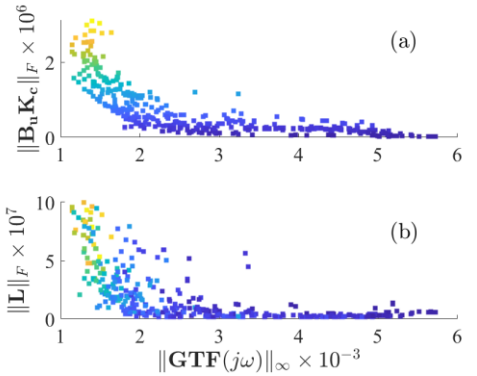

Figure 3. Projections of the Pareto Front. (a) $\|\mathbf{B_u K_c}\|_F$ versus $\|\mathbf{GTF}(j\omega)\|_\infty$, (b) $\|\mathbf{L}\|_F$ versus $\|\mathbf{GTF}(j\omega)\|_\infty$. The color code represents the levels of $\|\mathbf{B_u K_c}\|_F$ with red denotes the highest value, and dark blue denotes the lowest value.

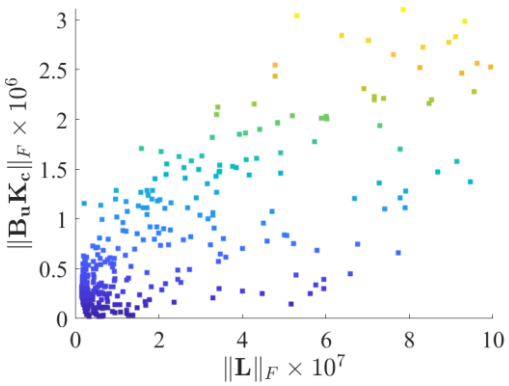

Figure 4. A 2D Projection of the Pareto Front. $\|\mathbf{B_u K_c}\|_F$ versus $\|\mathbf{L}\|_F$ .The color code represents the levels of $\|\mathbf{B_u K_c}\|_F$ with red denotes the highest value, and dark blue denotes the lowest value.

Stability Robustness

The profiles of the dominant open-loop pole $\lambda_{o_{\max}}$, closed-loop pole $\lambda_{c_{\max}}$, and estimator eigenvalue $\lambda_{e_{\max}}$ at the best and the worst stability robustness are shown in Figure 5, 6, and 7, respectively. Figure 5 shows the open-loop system is sensitive to the airspeed, V (*m/s*), and becomes more unstable when V increases. Figure 6 shows the profile of $\lambda_{c_{\max}}$ at different degrees of relative stability. As expected, the closed-loop system shows better relative stability at $\lambda_{c_{\max}} = -31.0577$ than that at $\lambda_{c_{\max}} = -10.1686$. At $\lambda_{c_{\max}} = -31.0577$, the closed-loop system become unstable near *V=238 m/s*. For $\lambda_{c_{\max}} = -10.1686$, the flutter occurs at approximately *V=218 m/s*. In active aeroelastic control, flutter must be placed outside the flight envelope of an aircraft. Typically, a 15% flutter free margin or more is needed beyond the design envelope for both civil and military aircrafts (Carey & Buttrill, 1996).

According to the flight rules in the US, no person may operate an aircraft below 10,000 feet MSL (Mean Sea Level) at an indicated airspeed of more than 250 knots (128.611 m/s). Based on this, we notice that the flutter boundaries is extended to more than 69% or ((218-128.611)/128.611 * 100) % beyond the design speed envelope when $\lambda_{c_{\max}} = -10.1686$. Thus, a unique control gain can be implemented for the whole flight. Figure 7 shows the profile of $\lambda_{e_{\max}}$ at different degrees of estimator relative stability. The estimator shows better relative stability at $\lambda_{e_{\max}} = -6.5623e+3$ than that at $\lambda_{e_{\max}} = -937.6681$. Also, we notice that the estimator dynamics will always be stable regardless the change in the air stream velocity. This is expected since the dominate estimator pole is placed to the left of the closed-loop fastest eigenvalue.

Time- Domain Response

For the velocity, *V=87.5 m/s* (onset of flutter), the closed loop and estimator response is computed when they are excited by a discrete "1-cosine" gust loading (Haghighat, Martins, & Liu, 2012). It is clear that the responses at $\min\left(\lambda_{c_{\max}}\right)$ (see Figure 8), min($\|\mathbf{GTF}(j\omega)\|_\infty$) (see Figure 10), max($\|\mathbf{B_u K_c}\|_F$) (see Figure 12), and max($\|\mathbf{L}\|_F$) (see Figure 14) are the best. While those at $\max\left(\lambda_{c_{\max}}\right)$ (shown in Figure 9), max($\|\mathbf{GTF}(j\omega)\|_\infty$) (shown in Figure 11) min($\|\mathbf{B_u K_c}\|_F$) (shown in Figure 13), and min($\|\mathbf{L}\|_F$) (shown in Figure 15) are the worst. But in all cases, the closed-loop control system can suppress the flutter and stabilize the system and the estimator converges quickly. Also, the simulations show that the first four states (q_1 to q_2) always converge to their true values and their first time derivatives take less than 1 second to converge. These responses also confirm the conflicting nature of the design objectives.

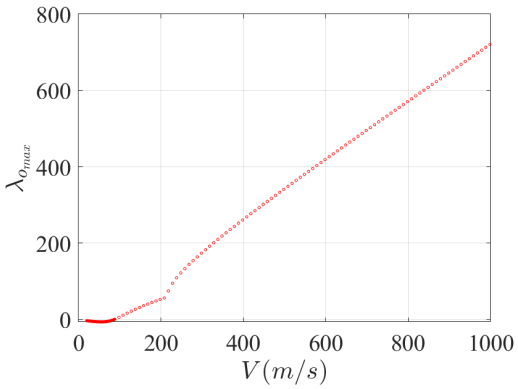

Figure 5. Profile of the Open-loop Poles, $\lambda_{o_{\max}}$, with Change in Airspeed

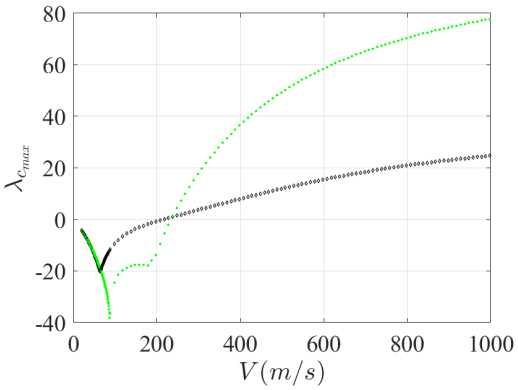

Figure 6. Profile of the Close-loop Poles, $\lambda_{c_{\max}}$, with Change in Airspeed. Green curve with * marker represents $\lambda_{c_{\max}} = -31.0577$. Black curve with diamond marker is the profile of $\lambda_{c_{\max}} = -10.1686$.

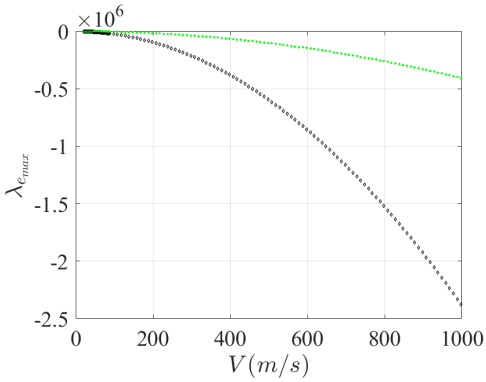

Figure 7. Profile of the Observer Poles, $\lambda_{e_{\max}}$, with Change in Airspeed. Green curve with * marker represents $\lambda_{e_{\max}} == -6.5623e+3$. Black curve with diamond marker is the profile of $\lambda_{e_{\max}} == -937.6681$.

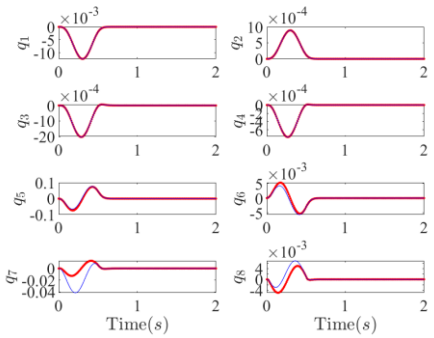

Figure 8. The Response of Control Surfaces at V=88 m/sec (red solid line: closed-loop response and blue solid line: estimator response at $\min\left(\lambda_{c_{\max}}\right)$.

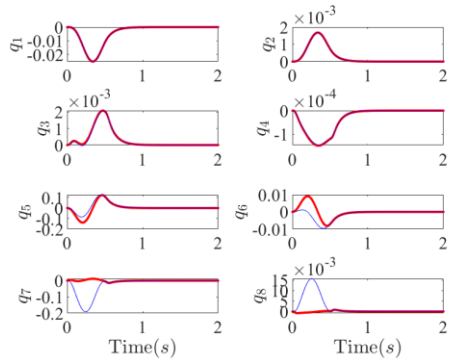

Figure 9. The Response of Control Surfaces at V=88 m/sec (red solid line: closed-loop response and blue solid line: estimator response at $\max\left(\lambda_{c_{\max}}\right)$.

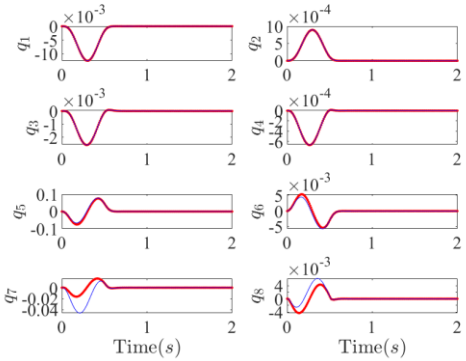

Figure 10. The Response of Control Surfaces at V=88 m/sec (red solid line: closed-loop response and blue solid line: estimator response at min($\|\mathbf{GTF}(j\omega)\|_\infty$).

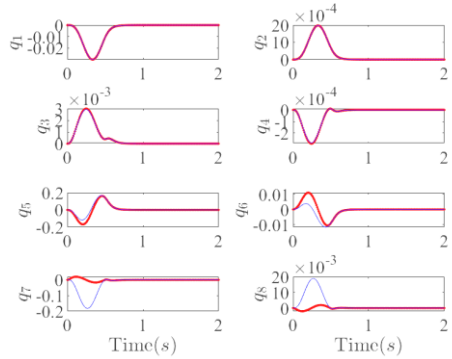

Figure 11. The Response of Control Surfaces at V=88 m/sec (red solid line: closed-loop response and blue solid line: estimator response at max($\|\mathbf{GTF}(j\omega)\|_\infty$).

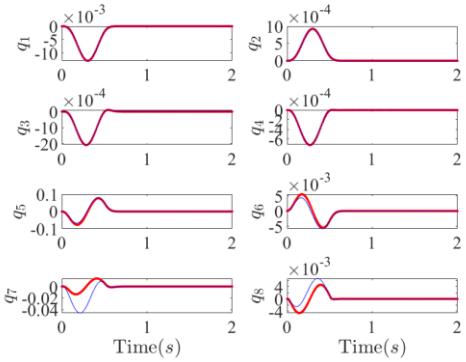

Figure 12. The Response of Control Surfaces at V=88 m/sec (red solid line: closed-loop response and blue solid line: estimator response at max($\|\mathbf{B_u K_c}\|_F$).

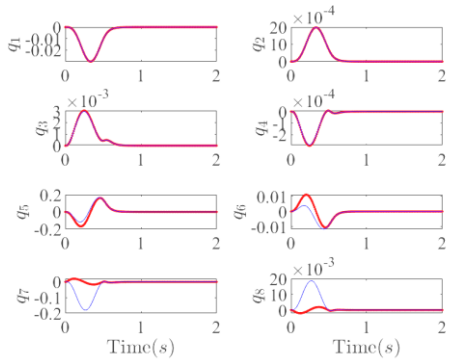

Figure 13. The Response of Control Surfaces at V=88 m/sec (red solid line: closed-loop response and blue solid line: estimator response at min($\|\mathbf{B_u K_c}\|_F$).

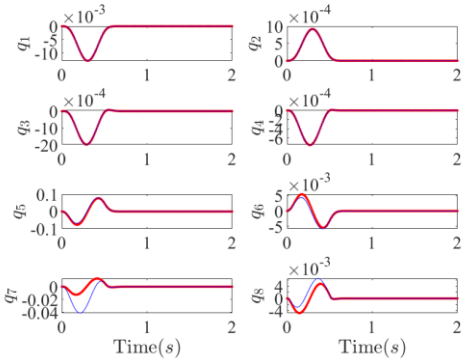

Figure 14. The Response of Control Surfaces at V=88 m/sec (red solid line: closed-loop response and blue solid line: estimator response at max($\|\mathbf{L}\|_F$).

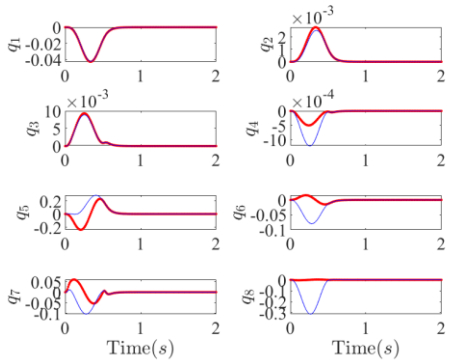

Figure 15. The Response of Control Surfaces at V=88 m/sec (red solid line: closed-loop response and blue solid line: estimator response at min($\|\mathbf{L}\|_F$).

Conclusion

We have studied the multidisciplinary and multi-objective optimal design of a wing with three control surfaces. The optimization problem with 15 design parameters and 4 objective functions is solved by NSGA-II algorithm. The decision variable space consists of 3 parameters related to the span wise and chord lengths of the control surfaces, 11 setup gains related to the LQR penalty matrices, and one parameter to place the estimator poles to the left of those of the closed-loop system. The objective space contains four objectives: minimization of the controlled system response to gust loads, and maximization of the closed-loop system's stability robustness, minimization of the control energy utilization, and minimization of the Frobenius norm of the estimator gains. The optimal trade-off solutions in terms of the Pareto set and front are obtained. The Pareto set includes multiple design options from which the decision-maker can choose to implement. The Pareto front demonstrates competing relationship between the design objectives. The poles of the closed-loop and observer eigenvalues versus airspeed for different levels of relative stability show that a unique control gain can be designed for the entire flight envelope.

Acknowledgements

This research was made possible by the NASA Established Program to Stimulate Competitive Research Grant # #80NSSC19M0054.

References

Brown, R. N., & Singh, K. V. (2015). Optimal sizing and configurations of the control surfaces for active aeroelastic control. *In AIAA Atmospheric Flight Mechanics Conference*, (p. 2241).

Brown, R. N., Singh, K. V., & Kolonay, R. M. (2017). Optimal sizing and placement of control surfaces for active aeroservoelastic control. *In 58th AIAA/ASCE/AHS/ASC Structures, Structural Dynamics, and Materials Conference*, (p. 0569).

Bryson, A. E. (2018). *Applied optimal control: optimization, estimation and control.* Routledge.

Carey, S., & Buttrill, S. (1996). *Aeroservoelastic Simulation of an Active Flexible Wing Wind Tunnel Model.* NASA Langley Technical Report Server.

Durillo, J. J., Nebro, A. J., Coello, C. A., Luna, F., & Alba, E. (2008). A comparative study of the effect of parameter scalability in multi-objective metaheuristics. *In 2008 IEEE Congress on Evolutionary Computation (IEEE World Congress on Computational Intelligence* (pp. 1893-1900). IEEE.

El Hajjaji, A., & Ouladsine, M. (2001). Modeling and nonlinear control of magnetic levitation systems. *IEEE Transactions on industrial Electronics, 48*(4), 831-838.

Haghighat, S., Martins, J. R., & Liu, H. H. (2012). Aeroservoelastic design optimization of a flexible wing. *Journal of Aircraft, 49*(2), 432-443.

Hu, X., Huang, Z., & Wang, Z. (2003). Hybridization of the multi-objective evolutionary algorithms and the gradient-based algorithms. *In The 2003 Congress on Evolutionary Computation, 2003. CEC'03*, (pp. 870-877).

Ishibuchi, H. Y. (2009). Evolutionary many-objective optimization by NSGA-II and MOEA/D with large populations. *IEEE International Conference on Systems, Man and Cybernetics*, 1758-1763.

Khot, N. S., K. Appa, and F. E. Eastep. (2000). Optimization of flexible wing without ailerons for rolling maneuver. *Journal of aircraft, 37*(5), 892-897.

Luenberger, D. G. (1964). Observing the state of a linear system. *IEEE transactions on military electronics*, 74-80.

MathWork. (2020, 07 15). *Pole Placement*. Retrieved from MathWork: https://www.mathworks.com/help/control/getstart/pole-placement.html#f2-1031415.

Nam, C., Chattopadhyay, A., & Kim, Y. (2000). Optimal wing planform design for aeroelastic control. *AIAA journal, 38*(8), 1465-1470.

Oral, Ö., Çetin, L., & Uyar, E. (2010). A Novel Method on Selection of Q And R Matrices In The Theory Of Optimal Control. *International Journal of Systems Control, 1*(2).

Pareto, V. (1971). Manual of Political Economy. *The MacMillan Press,London*.

Sardahi, Y. (2016). *Multi-objective optimal design of control systems* . (Doctoral dissertation, UC Merced).

Sardahi, Y. and Boker, A. (2018). Multi-Objective Optimal Design of Four-Parameter PID Controls. *ASME 2018 Dynamic Systems and Control Conference.* Atlanta, Georgia.

Singh, K. V., & McDonough, L. A. (2014). Optimization of Control Surface Parameters with Augmented Flutter Boundary Constraints. *In AIAA Atmospheric Flight Mechanics Conference*, (p. 2050).

Stanford, B. K. (2016). Optimization of an aeroservoelastic wing with distributed multiple control surfaces. *Journal of Aircraft, 53*(4), 1131-1144.

Tewari, A. (2002). Modern control design. In A. Tewari, *Modern control design* (pp. 283-308). NY: John Wiley & sons.

Tian, Y., Cheng, R., Zhang, X., & Jin, Y. (2017). PlatEMO: A MATLAB platform for evolutionary multi-objective optimization [educational forum]. *IEEE Computational Intelligence Magazine, 12*(4), 73-87.

Woźniak, P. (2010). Multi-objective control systems design with criteria reduction. *In Asia-Pacific Conference on Simulated Evolution and Learning*, (pp. 583-587). Springer, Berlin, Heidelberg.

APPENDIX A

According to (Singh & McDonough, 2014), the parameters and matrices for the system given in Eq. (1) are as follows:

$$\begin{aligned}
&\bar{c} = \left(c^2/2 - cx_f\right)\\
&\text{[illegible]} = \left(c^3/3 - c^2 x_f + c x_f^2\right)\\
&e_d = \sqrt{E_c\left(1-E_c\right)}\\
&b_c = a_w/\pi\left(1-E_c\right)e_d\\
&a_c = a_w/\pi\left(\cos^{-1}\left(1-E_c\right)+2e_d\right)
\end{aligned} \tag{A.1}$$

$$\mathbf{M} = m\begin{bmatrix} \bar{s}^5 c/5 & \bar{s}^6 c/6 & \bar{s}^4\bar{c}/4 & \bar{s}^5\bar{c}/5 \\ \bar{s}^6 c/6 & \bar{s}^7 c/7 & \bar{s}^5 c\bar{c}/5 & \bar{s}^6 c\bar{c}/6 \\ \bar{s}^4\bar{c}/4 & \bar{s}^5\bar{c}/5 & \bar{s}^3[illegible]/3 & \bar{s}^4[illegible]/4 \\ \bar{s}^5\bar{c}/5 & \bar{s}^6\bar{c}/6 & \bar{s}^4[illegible]/4 & \bar{s}^5[illegible]/5 \end{bmatrix}, \mathbf{C}_a = \begin{bmatrix} -ca_w\bar{s}^5/10 & -ca_w\bar{s}^6/12 & 0 & 0 \\ -ca_w\bar{s}^6/12 & -ca_w\bar{s}^7/14 & 0 & 0 \\ c^2 ea_w\bar{s}^4/8 & c^2 ea_w\bar{s}^5/10 & c^3 M_{[illegible]}\bar{s}^3/24 & c^3 M_{[illegible]}\bar{s}^4/32 \\ c^2 ea_w\bar{s}^5/10 & c^2 ea_w\bar{s}^6/12 & c^3 M_{[illegible]}\bar{s}^4/32 & c^3 M_{[illegible]}\bar{s}^5/40 \end{bmatrix} \tag{A.2}$$

$$\mathbf{C} = \mathbf{0}, \mathbf{K} = \begin{bmatrix} 4EI\bar{s} & 6EI\bar{s}^2 & 0 & 0 \\ 6EI\bar{s}^2 & 12EI\bar{s}^3 & 0 & 0 \\ 0 & 0 & GJ\bar{s} & GJ\bar{s}^2 \\ 0 & 0 & GJ\bar{s}^2 & 4GJ\bar{s}^3/3 \end{bmatrix}, \mathbf{K}_a = \begin{bmatrix} 0 & 0 & -ca_w\bar{s}^4/8 & -ca_w\bar{s}^5/10 \\ 0 & 0 & -ca_w\bar{s}^5/10 & -ca_w\bar{s}^6/12 \\ 0 & 0 & c^2 ea_w\bar{s}^3/6 & c^2 ea_w\bar{s}^4/8 \\ 0 & 0 & c^2 ea_w\bar{s}^4/8 & c^2 ea_w\bar{s}^5/10 \end{bmatrix} \tag{A.3}$$

$$\mathbf{F}_c = \rho V^2 c\begin{bmatrix} & & & \\ -a_c s_1^3/6 & -a_c\left(s_2^3 - s_1^3\right)/6 & -a_c\left(\bar{s}^3 - s_2^3\right)/6 & \\ -a_c s_1^4/8 & -a_c\left(s_2^4 - s_1^4\right)/8 & -a_c\left(\bar{s}^4 - s_2^4\right)/8 & \\ cb_c s_1^2/4 & cb_c\left(s_2^2 - s_1^2\right)/4 & cb_c\left(\bar{s}^2 - s_2^2\right)/4 & \\ cb_c s_1^3/6 & cb_c\left(s_2^3 - s_1^3\right)/6 & cb_c\left(\bar{s}^3 - s_2^3\right)/6 & \end{bmatrix}, \mathbf{F}_g = \rho V c\begin{bmatrix} & & & \\ -a_c s_1^3/6 & -a_w\left(s_2^3 - s_1^3\right)/6 & -a_w\left(\bar{s}^3 - s_2^3\right)/6 & \\ -a_w s_1^4/8 & -a_w\left(s_2^4 - s_1^4\right)/8 & -a_w\left(\bar{s}^4 - s_2^4\right)/8 & \\ ces_1^2/4 & ce\left(s_2^2 - s_1^2\right)/4 & ce\left(\bar{s}^2 - s_2^2\right)/4 & \\ ces_1^3/6 & ce\left(s_2^3 - s_1^3\right)/6 & ce\left(\bar{s}^3 - s_2^3\right)/6 & \end{bmatrix}, \tag{A.4}$$

Table A.1. Aeroelastic system parameters for the wing having three control surfaces

Parameter	Symbol	Value	Parameter	Symbol	Value
Semi-span (m)	$\bar{s}$	6	Unsteady torsional velocity term	$M_{[illegible]}$	-1.2
Chord (m)	c	1	Eccentricity ratio	e	0.15
Mass per unit area (kg/m^2)	m	10	Position of flexural axis	x_f	$0.4c$
Air density (kg/m^3)	ρ	1.225	Flexural rigidity	EI	400×10^3
2D lift curve slope	a_w	2π	Torsional rigidity	GJ	200×10^3